

Dispersion processes in weakly dissipative estuaries: Part 1. Single harmonic tide.

A. De Leo¹, N. Tambroni¹, and A. Stocchino²

¹Dipartimento di Ingegneria Civile, Chimica e Ambientale, Università degli Studi di Genova, via
Montallegro 1, 16145, Genova, Italia

²Department of Civil and Environmental Engineering, Hong Kong Polytechnic University, Hung Hom,
Kowloon, Hong Kong

Key Points:

- Time dependent flow and the residual current forced by tides is studied in a large-scale physical model of a compound tidal channel.
- Large scale vortices show a complex dynamical behavior that varies with the amplitude and the period of the forcing tides.
- Different dispersion regimes are observed depending on the forcing tide, yielding to a strong variability of the diffusion coefficient.

Corresponding author: Annalisa De Leo, annalisa.deleo@edu.unige.it

Abstract

We report the results of an extensive experimental campaign dedicated to the analysis of turbulent dispersion owing to the circulations in tide dominated estuaries, characterized by a compound cross section (a main channel and lateral tidal flats). Following the classification suggested by Toffolon et al. (2006), we concentrate our attention on weakly-convergent and weakly-dissipative estuaries, where the internal waters communicate with the open sea through an inlet mouth. Particle Image Velocimetry is employed to measure two-dimensional surface velocity. Large scale macro-vortices, generated by vortex shedding during the flood phase from the inlet barrier, tend to occupy the entire tidal flats width and, irrespective of the controlling parameters, they are completely flushed out during the ebb phase. Flow decomposition based on averaging over the tidal period enlightens the presence of an intense residual current, with shape influenced by the large-scale flood vortices. The measured Eulerian surface velocity fields form the basis for a thorough Lagrangian analysis, which yields a clear picture of the dispersion regimes. The presence of large-scale vortices and of an intense residual current strongly influences the Lagrangian auto-correlation functions and the corresponding absolute dispersion time evolution. Looping auto-correlations are the signature of both the periodic forcing and vortices, ultimately, leading to super diffusive regimes. Moreover, an asymptotic Brownian regime is always found for the investigated range of parameters allowing for an estimate of the horizontal dispersion coefficients. For the latter, we suggest a simplified algebraic formulation that well fits the experimental estimates.

Plain Language Summary

Estuaries are unique environments where inland freshwater carried by rivers meets salty and warmer sea waters. The encounter of masses of water with such different characteristics makes estuaries an extremely dynamic environment suitable for the proliferation of a great variety of ecosystems and biodiversity. Owing to their strategic geographical position estuaries have been and still are regions of great development for human society. This poses new questions on the environmental impact of human activities and their potential pressures. In this work, we investigate the dispersion processes using a large scale physical model of natural estuaries, bounded by an inlet mouth, where tides are the dominant drivers. A great effort has been devoted to trying to classify the behaviors of natural estuaries based on several physical characteristics and to estimate typical transport time scales. Here, we aim to analyze the dispersion regimes relying on 2D velocity measurements at the free surface used as a basis for a Lagrangian analysis. We will show how the presence of a tidal inlet generates complex flow patterns even with a monochromatic tide. The resulting residual current is the main responsible for a net longitudinal dispersion that can reach high values of the corresponding dispersion coefficients.

1 Introduction

Estuaries are classically defined as a semi-enclosed and coastal body of water, communicating to the open sea, where freshwater coming from inland mixes with sea water (Pritchard, 1956). The resulting density gradients (horizontal and vertical) have been found as a major circulation driver in estuarine environments (MacCready & Geyer, 2009; Geyer & MacCready, 2014). However, this original definition excludes several estuarine configurations where freshwater input is negligible (Viero & Defina, 2016) or even absent for several months as for arid, tropical and subtropical basins. A great effort has been also devoted to classifying estuarine regions depending on their geomorphology, density stratification or on the typical hydrodynamics (Valle-Levinson, 2010). Considering the latter feature, circulation in estuaries and coastal bays is mainly driven by baroclinic pressure gradients, tidal induced currents (periodic and stationary), wind stress and river

inflow and the consequent plume. From a hydrodynamic point of view, tidal propagation within estuaries has received a great attention in the attempt to find the best physical parameters to describe them (Seminaro et al., 2010; Toffolon et al., 2006; Cai et al., 2012). The role of tidal circulation in estuarine mixing has been considered of less importance for several decades (Geyer & MacCready, 2014). However, the so-called residual currents derived by averaging over a tidal period are now recognized to be a fundamental driver for mass transport and dispersion processes (Jay, 1991; Zimmerman, 1986) owing to the strong and persistent straining and shearing (Ridderinkhof & Zimmerman, 1992). The time periodic character of the tides also generates dispersion mechanisms sustained by different flow scales especially if related to the complex geometry of the real estuaries. Several field measurements of longitudinal dispersion coefficient report a wide range of values, spanning almost two order of magnitudes from 10 to $10^3 \text{ m}^2/\text{s}^{-1}$ (Fischer et al., 1979; Monismith et al., 2002; Lewis & Uncles, 2003; Banas et al., 2004). Moreover, tides tend to produce no monotonic particle velocity correlation and Lagrangian integral time scales as in classical statistically steady or homogenous turbulence (Enrile et al., 2019) leading to possible particle looping trajectories. Looping-like particle trajectories have been also studied in oceanic context and they are found to be related to particular dispersion regimes (Berloff et al., 2002; Veneziani et al., 2004; Enrile et al., 2019).

Two of the main open issues concern with the definition of typical transport time scales, relevant for dispersion and water quality issues and the estimate of the dispersion coefficients that control longitudinal transport. Seeking a reliable definition of the time scale for transport processes has led to use different measure such as residence time, flushing time, age (see Cucco et al. (2009); Umgiesser et al. (2014); Viero and Defina (2016); Yang et al. (2018) among many others). The tentative is to classify estuaries based on these time scales and an example can be found in Umgiesser et al. (2014) where several estuaries and coastal bays of the Mediterranean Sea have been compared. However, most of these time scales are based on Eulerian concepts and quite a few on a Lagrangian approaches. Surprisingly, classical analyses in terms of single and multiple particle statistics are very seldom applied to estuaries compared to oceanographic and atmospheric applications (LaCasce, 2008). Attempts to study the dispersion processes under controlled laboratory conditions in estuaries are very limited in literature (Kusumoto, 2008; Dronkers, 2019) although worth pursuing. In fact, controlled experiments with simple boundary conditions provide a check of some of the main mechanisms which drive the dispersion process, a goal quite difficult to achieve on the basis of field observations whose interpretation is generally complicated by the large scale of the processes, the more irregular natural geometries and the simultaneous presence of a variety of features whose role cannot be readily isolated. Moreover they provide an useful dataset to test reliability of analytical and numerical models. In the present study, we aim to investigate the relevant dispersion processes using a large scale physical model of a weakly-dissipative tide dominated estuary (following the classification proposed by Toffolon et al. (2006)) characterized by the presence of an inlet mouth that connects the outer sea to a compound tidal channel. Flow is forced by tidal variation imposed at the outer basin. Real tides are made of multiple constituents, semi-diurnal and diurnal, generated by different astronomical forcing, solar and moon tides. In an attempt to understand the role of the tidal constituents, we have designed this study with the aim to firstly investigate the role of a single harmonic, objective of Part 1, and separately the role of two harmonics, representing the semi-diurnal and diurnal components, with varying amplitudes (Part 2 of the study). In Part 1, we provide a detailed description of the transient macro-vortices generated at the inlet and the resulting residual current. The generation of flood-vortices is compared with previous works (Nicolau del Roure et al., 2009) and extended considering the effect of the vorticity generation owing to the depth jump between the channel and the tidal flats (Brocchini & Colombini, 2004; Stocchino et al., 2011). Large scale Particle Image Velocimetry is employed to measure two dimensional surface velocity fields providing a high spatial and temporal description of the flow. A detailed Lagrangian anal-

ysis of the typical integral scales and single particle statistics, varying the controlling parameter, is performed and provides a clearer picture of the processes occurring in weakly-dissipative estuaries. Finally, an analytic formula for the horizontal diffusion coefficient as a function of the friction parameter is suggested in a simple form. We leave for Part 2 the effects on the dispersion regimes in the case of two harmonics tides and the comparison with the one constituent case.

2 Experimental set-up and measuring techniques

The experiments were performed in a physical model in the hydraulic Laboratory of the Department of Civil, Chemical and Environmental Engineering of the University of Genova, Italy. A sketch of the overall experimental setup is shown in Figure 1. The experimental apparatus consists of a tidal channel, closed at one end and connected to a rectangular basin, representing the sea, at the other end. The tidal channel (23 m long) is characterized by a symmetrical compound cross-section with a deep main channel and lateral flats with an overall width equal to $w_{ch} = 2.42$ m. The main channel has a 2.5‰ longitudinal slope and a rectangular cross section with a landward decreasing width, starting from about 70 cm at the tidal inlet (w_i) reaching about 11 cm at the channel end. Consequently, the two tidal flats have a varying width between 0.86 m and 1.16 m on each side. The main channel has a constant depth of 0.24 m. The basin is 6 m long and 2.20 m wide (w_b), with a maximum depth $h_b = 0.5$ m. Contrary to the tidal channel, the bottom of the basin is horizontal. Tidal flats are closed at the inlet through two thin vertical plates ($l_i = 0.86$ m) which separate them from the outer sea-basin. Hence water exchange between the basin and the channel is allowed only at the inlet cross section of the main tidal channel. The inlet opening has been maintained unaltered during the experimental campaign. The estimate of the conductance coefficient C is about 12, which corresponds to a Manning’s resistance coefficient of about $0.0167 \text{ sm}^{-1/3}$. The present experiments have been performed keeping a constant mean water depth equal to 0.36 m at the channel inlet. A monochromatic tide has been reproduced by imposing regular volume waves with variable period and amplitude, generated by the periodic motion of an oscillating cylinder inside an adjacent feeding tank. The cylinder is remotely controlled using a digital signal acquisition/ generation system and a time law of the kind $\eta = a \sin(\omega t)$, where t is the time, η is the free surface elevation, a the tidal amplitude and ω the tidal angular frequency also equal to $\omega = 2\pi/T$ with T being the tidal period. To minimize wave reflections, a dissipative sloping mound was installed at the end of the channel. During each experiment, water level and surface velocities have been measured. In particular, free surface elevation was monitored using four ultrasound gauges (Honeywell model 946-A4V-2D-2C0-380E, with 30 cm range and an accuracy of 0.2% of the full scale), placed on the axis of the channel respectively at a distance of 0, 4.75, 14.3 and 25 m from the wave maker (see Figure 1). Large Scale Particle Image Velocimetry (LS-PIV) was employed to measure the two-dimensional time dependent surface velocity fields $\mathbf{u}(x, y, t) = (u(x, y, t), v(x, y, t))$, where, according to the notations of Figure 1, we denote by x the landward oriented longitudinal axis of the channel and by y the lateral coordinate with origin located in the basin at a distance of 3 m from the channel inlet; u and v are the x and y components of the velocity \mathbf{u} , respectively. It is worth noting that, the large dimension of the interested area imposes specific equipment modifications with regards to the standard PIV technique. The channel water surface was densely and uniformly seeded by polyethylene particles (940 kg m^{-3} , mean dimension 3 mm) used as PIV tracers. LS-PIV acquisitions were recorded employing five high-resolution GigaEthernet digital camera (Teledyne Dalsa Genie Nano C1280 and C2450). Depending on the camera model, the resolutions varied between 2448×2048 pixels and 1280×1024 pixels. 6-mm lens have been mounted on the cameras. Cameras were fixed on rigid supports placed at an elevation of 4 m from the bottom of the channel, pointing downwards, as shown in Figure 1. Based on the camera arrangement, the field of view (FoV) for the velocity measurements was such to cover a large area, including the inlet region, of about

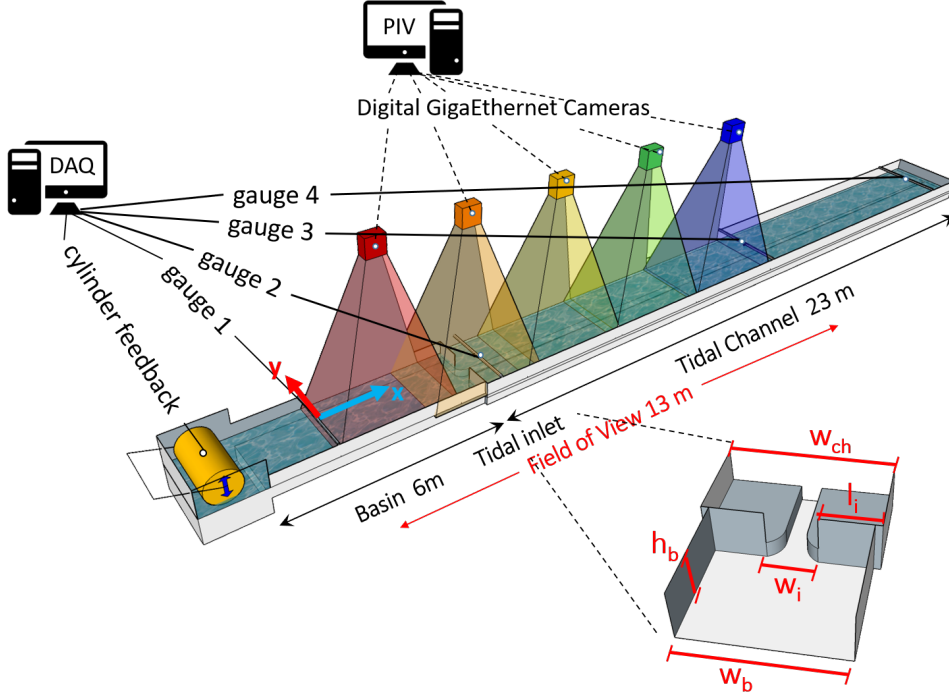


Figure 1. Sketch of the experimental set up and measuring systems.

13 × 2 m, extending from about the last 3 m of the basin to about the first 10 m of the channel for the entire width, with cameras overlapping in the longitudinal direction of about 20 %. Lighting was produced using eight 500W white light halogen lamps. The LS-PIV acquisition frame rate was set equal to 10 fps. A single acquisition lasted for about five tidal periods and, thus, each camera recorded between 5000 and 9000 images, depending on the experimental parameters. The images from the five digital cameras have, then, been processed in order to obtain a single panoramic image of the entire FoV before PIV analysis, performed using the software proVision-XSTM (Integrated Design Tools Inc).

A total of 20 experiments have been performed varying the tidal period and amplitude, see Table 1 for the relevant experimental parameters. Note that experiments from 1 to 7 were used to test and set the experimental apparatus and parameters.

3 Scaling arguments and estuary classification

Dealing with large scale geophysical problems such as hydrodynamics and mixing processes poses several challenges especially when the approach is based on laboratory experiments. The typical dimensions of real estuaries and tidal channels are usually of the order of several kilometers in the longitudinal and, possibly, in the transverse direction, and of several meters along the vertical. Thus, a proper scaling is necessary in order to avoid spurious effects owing to the small scale of the laboratory facilities compared with the prototype. In this section, we focus our attention on two main aspects: which is the correct similitude to adopt and to what extent our measurements are transferable to realistic context. Regarding the similitude, it is of paramount importance to firstly define which are the physical parameters relevant to our process. The definition of the correct dimensionless parameters for the hydrodynamic behavior of estuaries has been

Table 1. Main experimental parameters and *external* parameters as reported in Toffolon et al. (2006).

exp.	a [m]	R_h [m]	T [s]	R_e	χ	γ
8	0.003	0.086	160	9485	0.06	1.02
9	0.005	0.085	160	20923	0.11	1.02
10	0.007	0.085	160	25845	0.16	1.02
11	0.010	0.085	160	29981	0.23	1.02
12	0.012	0.086	160	35902	0.27	1.02
13	0.002	0.087	100	17881	0.02	0.64
14	0.004	0.086	100	30853	0.06	0.64
15	0.007	0.086	100	33837	0.10	0.64
16	0.011	0.085	100	30984	0.15	0.64
17	0.017	0.086	100	43470	0.23	0.64
18	0.002	0.083	130	13783	0.03	0.83
19	0.003	0.084	130	23452	0.05	0.83
20	0.005	0.085	130	30541	0.08	0.83
21	0.007	0.086	130	36422	0.12	0.83
22	0.009	0.086	130	44764	0.15	0.83
23	0.002	0.084	180	8172	0.06	1.15
24	0.004	0.085	180	15930	0.10	1.15
25	0.006	0.085	180	14287	0.14	1.15
26	0.008	0.086	180	27268	0.19	1.15
27	0.010	0.086	180	35195	0.24	1.15

long debated in the literature. Several attempts to found simple scaling of the main processes have been presented by Jay (1991), Savenije (1993) and Lanzoni and Seminara (1998) among others. However, as noted by Toffolon et al. (2006), the selected parameters in the cited studies mixed different parameters with scales that depend on the evolution of the process itself, whereas Toffolon et al. (2006) defined the governing parameters of the process based on external quantities. Note that as *external* we intend quantities based simply on the geometry of the domain and on the main characteristics of the tidal forcing. Therefore, we decided to follow the approach by Toffolon et al. (2006) using their convergence ratio parameter (γ), that is related to the planimetric scales of the estuary, and the friction parameter (χ), defined as the ratio between friction and inertia. These two dimensionless parameters are written as:

$$\gamma = \frac{L_g}{2\pi L_b}, \quad \chi = \epsilon \frac{L_g}{2\pi C^2 R_h}, \quad \text{with} \quad L_g = T\sqrt{gR_h}, \quad (1)$$

where $\epsilon = a/R_h$ is the non dimensional tidal amplitude, R_h is the mean hydraulic radius of the channel and L_b is the convergence length. Differently from the original definition, we have introduced the hydraulic radius instead of the mean flow depth D , which is more appropriate for complex cross-sections with tidal flats.

Based on the above choice, we have decided to design the present experiments preserving the friction to inertia ratio χ and to impose a scale distortion along the three coordinates. Scaling arguments will be resumed in the Section 5.2, where we describe the dispersion regime with the aim to extend the laboratory measurements to natural estuaries scales.

Since we have imposed a similitude based on the parameter χ , we are now interested to understand what kind of estuaries we are representing in our experiments based on the classification reported in Toffolon et al. (2006). Figure 2 shows the values of the

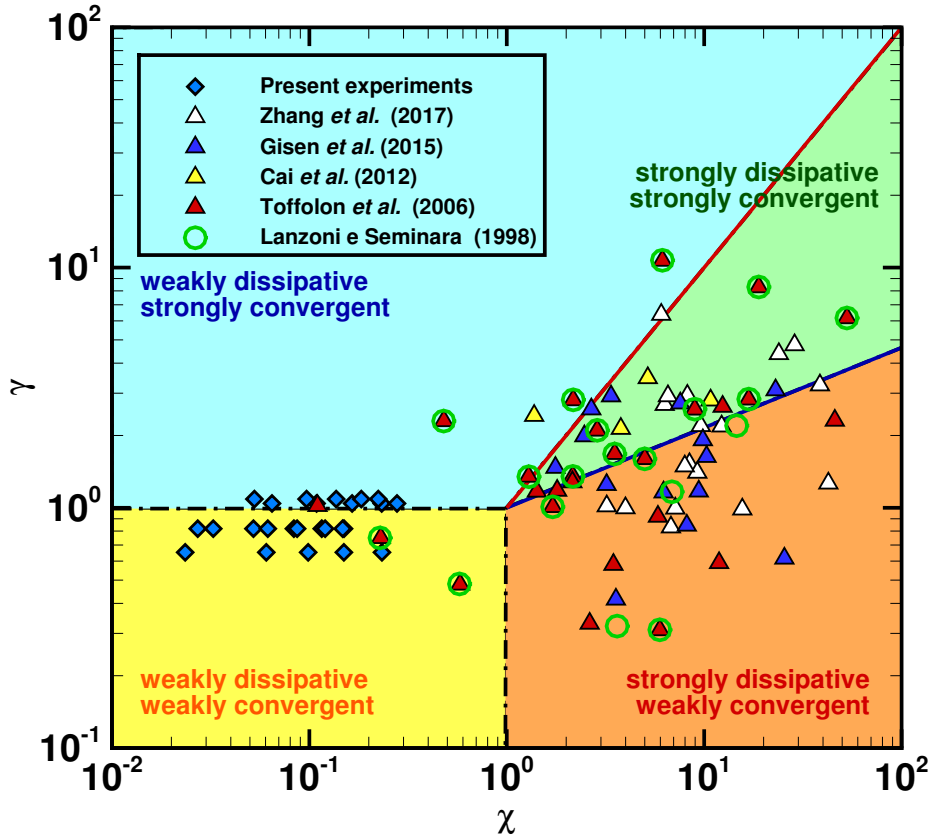


Figure 2. (χ, γ) -plane classification of several natural estuaries as reported in Lanzoni and Seminara (1998), Toffolon et al. (2006), Cai et al. (2012) Gisen and Savenije (2015) and (Zhang & Savenije, 2017), together with the present experiments. The thick red line represents the $\gamma = \chi$ boundary, whereas the thick blue solid line the $\gamma = \chi^{1/3}$ law.

parameters χ and γ of several real estuaries (Toffolon et al., 2006; Lanzoni & Seminara, 1998; Cai et al., 2012; Gisen & Savenije, 2015; Zhang & Savenije, 2017) together with those associated to the present experiments. Depending on the values of γ and χ estuaries fall in one of the four different parameter regions, being namely weakly/strongly dissipative and weakly/strongly convergent. The red solid line indicates the case $\gamma = \chi$ meaning that gravity and inertia have exactly the same weight and the blue solid line represents the condition $\gamma = \chi^{1/3}$ whereby the gravitational effects balance the frictional ones (Toffolon et al., 2006). Our experiments (blue diamonds) fall in the weakly dissipative and weakly convergent region close to the boundary $\gamma = 1$, that represents the balance between friction and inertia. Thus, the measurements presented in the rest of the paper can be considered representative of the behavior of a real weakly dissipative estuaries with an almost constant channel width. Finally, note that in our physical model the channel has lateral tidal flats that might play an important role in the hydrodynamic and dispersion processes.

4 Eulerian analysis: time dependent flow and the generation of a residual current

In the present experiments, flow is forced by a given free surface tidal oscillation at one end of the flume, mimicking the effect of astronomical tides at open sea far from the estuary inlet. The periodic character of the forcing tide induces an unsteady flow field whose intensity and characteristics depend on tide propagation within the estuary. In general, the velocity field is three dimensional. Here we collect 2D free surface velocity fields which are a good approximation of the real flow field, because shallow water approximation is usually assumed valid owing to the strong scale separation between the vertical and planimetric dimensions. Moreover, the presence of an inlet always induces the generation of large-scale shallow vortices owing to the emission of vorticity at its corners and the consequent development of shear layers (Nicolau del Roure et al., 2009; Vouriot et al., 2019). These macro-vortices are recognized to be 2D structures being much wider than deep (Jirka, 2001) able to control the momentum, mass and sediments exchanges between the estuary and the outer sea (Wells & van Heijst, 2004; Blondeaux & Vittori, 2020). Dispersion is also influenced by another process typical of periodic flows in estuaries that plays a fundamental role over time scales of many tidal cycles, the so called residual current that can be revealed applying a temporal decomposition (Jay, 1991; Valle-Levinson, 2010). In the present experiments, by taking the average of the free surface flow fields over a tidal period T , a corresponding steady current, whose intensity and shape strongly depend on the external parameters and on the geometry of the estuary, occurs. Note that, as it will be discussed below, the 3D character of the flow field and the secondary flows, which in general are less important and limited to the bottom, are instead responsible for the presence of the observed occurrence of the free surface residual current at the channel inlet. In this section we will firstly discuss the 2D free surface unsteady flow and the consequent generation of inlet macro-vortices and, secondly, the characteristics of the 2D free surface residual currents.

4.1 Time dependent velocity fields and the dynamics of inlet macro-vortices

We firstly analyze the measured two-dimensional Eulerian free surface velocity fields $\mathbf{u}(\mathbf{x}, t)$, obtained from the large scale PIV measurements, with the aim to distinguish regions with different dynamical properties. To this end, the Eulerian fields have been post-processed with the aim to identify vortical structures. Among the many techniques of vortex identification, we employed the method based on the evaluation of the Okubo-Weiss parameter (Okubo, 1970; Weiss, 1991). For steady or slowly time dependent flows, the Okubo-Weiss criterion makes use of the eigenvalues of the local velocity gradient tensor \mathbf{D} , which can be written as $\mathbf{D}^2 = \lambda_0 \mathbf{I}$, where the Okubo-Weiss parameter $\lambda_0 = -\det(\mathbf{D})$ is the product of the eigenvalues of \mathbf{D} . However, it is better to write it in the form suggested by Weiss (1991) as $\lambda_0 = \frac{1}{4}(S^2 - \omega^2)$ where $S^2 = S_n^2 + S_s^2$ is the total square strain, sum of the normal (S_n) and shear (S_s) components, and ω^2 is the square vorticity. The sign of λ_0 discriminates between locally hyperbolic flow regions ($\lambda_0 > 0$ strain dominated) and locally elliptical flow regions ($\lambda_0 < 0$ rotation dominated). The latter are signature of coherent vortices.

Figure 3 reports examples of the 2D velocity fields with contours of the Okubo-Weiss parameter for the experiment 26. In particular, panels a1)-d1) show four snapshots taken during the flood phase, while panels a2)-d2) refer to the ebb phase. To help the identification of the main flow structures, we have focused on the area around the inlet, located at $x = 4$ m. Note that the geometry of the inlet used in the present study is identical to the *barrier island* analyzed in Nicolau del Roure et al. (2009). In their study, however, the Authors tested different others configurations of the inlets in a shallow basin without tidal flats with the aim to understand the trajectory of the vortex cores during a tidal cycles. In the present case, the generation of the macro-vortices during the flood phase is found to be controlled by the inlet corners that act as a source of vorticity that

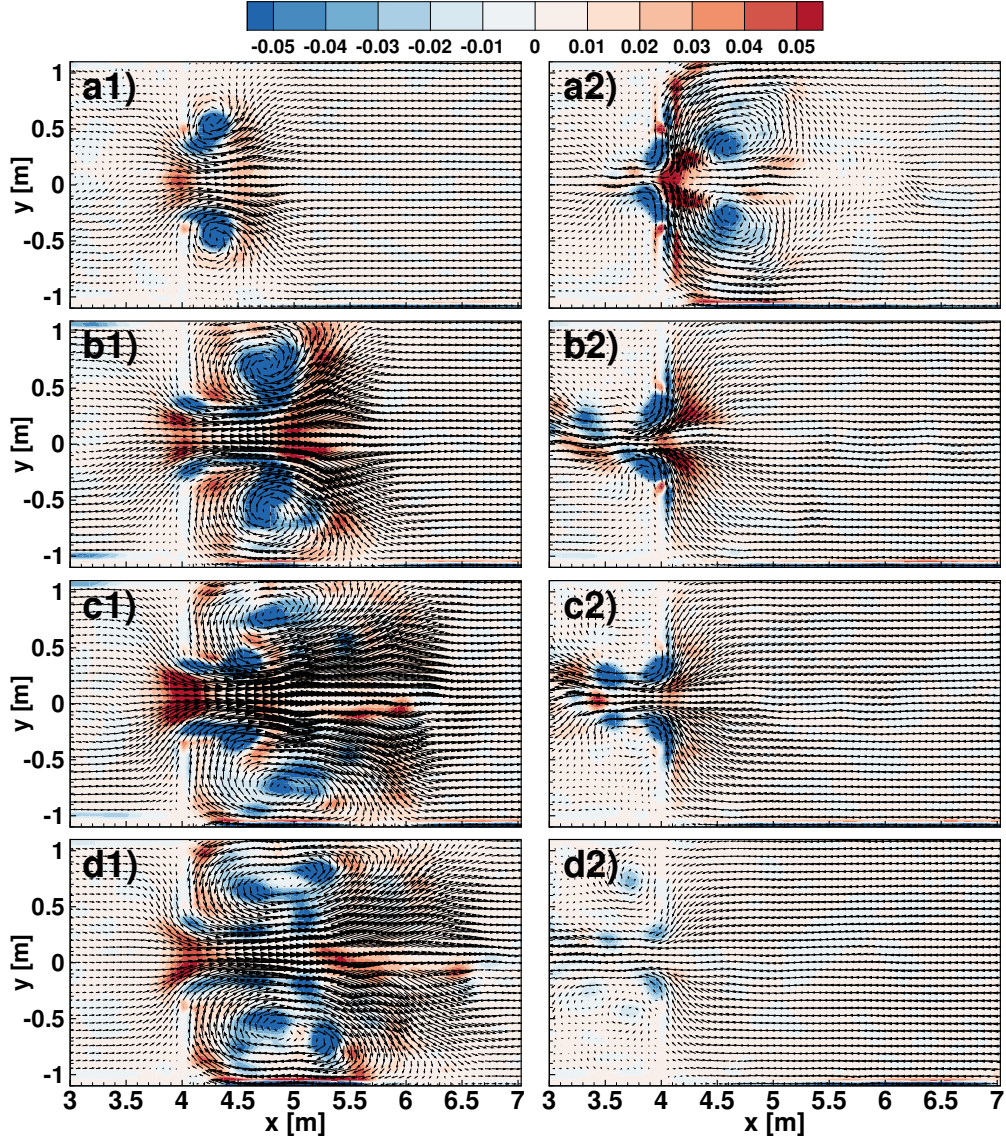


Figure 3. Free surface velocity fields at different times with superimposed the contours of the Okubo-Weiss parameter λ_0 . Panels a1)-d1) during the flood phase and panels a2)-d2) during the ebb phase. Note that domain reported is restricted to the region around the inlet. Data from Experiment 26.

is then convected towards the tidal channel. From the time sequence shown in Figure 3 from a1) to d1), it is clearly visible that small scales vortices are emitted with a period much shorter than the tidal one and, more interestingly, they tend to merge forming the larger structures that occupy the entire tidal flats width, leaving a strong jet in the center-line of the channel (red regions for $\lambda_0 > 0$). The mechanism of vortex merging is shown in detail in the movie provided as supplementary material. The mechanisms leading to the observed macro-vortices generation were already pointed out by Nicolau del Roure et al. (2009), who described it as the entrainment of small scales vortices in the main vortical structure. When a compound geometry is considered, the depth gradient between the tidal flats and the main channel is a further source of vorticity generation. This feature has been investigated by Brocchini and Colombini (2004), who derived the

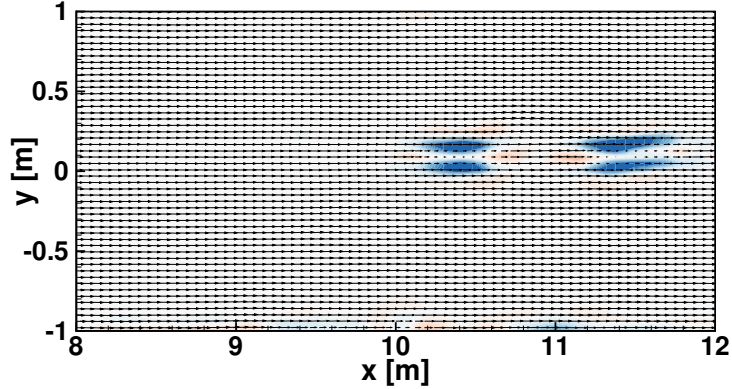


Figure 4. Example of the observation of transitional vortices at the flow depth jump between the main channel and the tidal flat. Vortices shown by negative values of the Okubo-Weiss parameter. Data from Experiment 17.

vorticity and enstrophy equations for shallow flows giving rise to new terms proportional to the span-wide depth jump. This mechanism is fundamental for the generation of macro-vortices in turbulent uniform flows (Stocchino & Brocchini, 2010; Stocchino et al., 2011) and, also in case of periodic forcing as in our experiments, it could sustain the vorticity generated at the inlet and along the main channel. However, in the periodic flow case, differently from the uniform channel flow conditions, these vortices are transient structures depending on the intensity of the flood/ebb flow within the channel and far from the inlet. Figure 4 shows an example of these vortices in the transition region between the tidal flats and the main channel. It is worth noting that in our experiments the values of depth ratio parameter $r_h = y_{mc}/y_{tf}$, defined as the ratio between the water depth in the main channel y_{mc} and the water depth in the tidal flat y_{tf} (Stocchino et al., 2011), vary according to the free surface variations in a tidal cycle, but are always larger than 3. This suggests that namely all experiments are in *shallow water* conditions. Notwithstanding this, the inversion of the longitudinal velocities might be the reason of the transient behavior of the transitional vortices. As far as the typical dimensions of the inlet macro-vortices are concerned, they are bounded on the span-wise direction between the main channel and the side walls, whereas their stream-wise extension depends on the intensity of the mean flow and, ultimately, on the friction parameter χ . In fact, the vortices are found to be strongly elongated in the longitudinal direction and to scale from 1 to 5 l_i . During the ebb phase, see panels a2)-d2), an intense outward jet is formed and penetrates into the basin for few meters. The jet is highly turbulent and small scale vortices are generated and transported with the jet. Moreover, for the range of parameters investigated, the flood macro-vortices are always flushed away during ebb. The condition by which the flood-vortices are flushed or trapped in the channel within a tidal period is usually described in terms of a Strouhal number, defined as $S_t = L/UT$, where L is a typical length scale related to the vortex shedding generation, U is a convective velocity scale and T is the tidal period. The importance of the role of the Strouhal number or its inverse, namely the Keulegan-Carpenter parameter, in the dynamics of the tidal macro-vortices or vortices generated by headlands has been recognized by several Authors (Signell & Geyer, 1991; Davies et al., 1995; Wells & van Heijst, 2004; Nicolau del Roure et al., 2009; Vouriot et al., 2019). In contexts similar to the present one, Wells and van Heijst (2004) defined three classes of vortices depending on S_t built with the inlet width and the tidal peak velocity. In particular a critical value, $S_{tc} = 0.13$, discriminates between vortices that are completely flushed away in a tidal cycle ($S_t < S_{tc}$) and

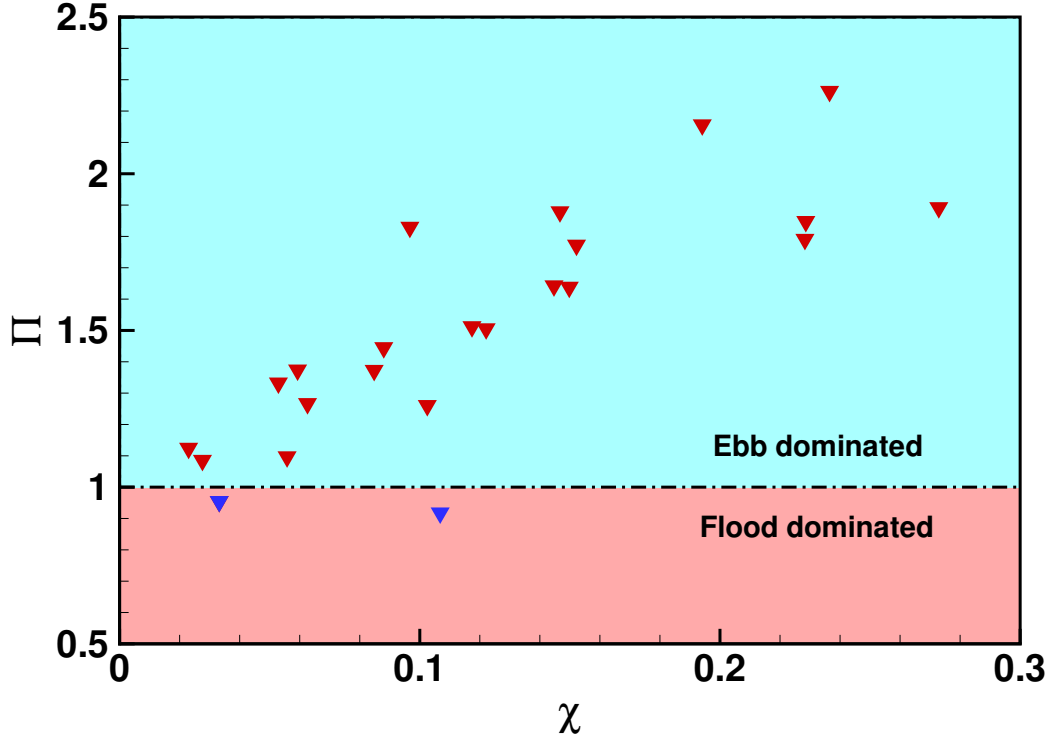


Figure 5. Ebb-Flood dominance classification based on the value of the power ratio Π as a function of the parameter χ .

vortices that do not completely decay within a cycle ($S_t > S_{tc}$). In the present case, we obtain values of S_t that exceed 0.13 only for the lowest tidal amplitude (exp. 8, 13, 18 and 23). However, even in those cases the flood-vortices are flushed away in the ebb phase, contrary to the observation of Wells and van Heijst (2004), Nicolau del Roure et al. (2009) and Vouriot et al. (2019). A possible explanation could be found in the compound geometry that enhances ebb velocities. The presence of tidal flats has been thus indicated as a source of ebb dominance (Kang & Jun, 2003). Different parameters can be used to evaluate the ebb/flood asymmetry in tidal flows, e.g. ebb time (Kang & Jun, 2003). In the present study, we have employed the tidal power per unit mass P defined as the time integral of the kinetic energy per unit mass. We have thus calculated the tidal powers associated to the flood and ebb phases separately and then estimated the ratio $\Pi = P_{ebb}/P_{flood}$ which indicates ebb or flood dominance whether it assumes values greater or lower than unity. The tidal asymmetry relative to the present experiments is shown in Figure 5 where Π is reported as a function of χ . Within the experimental errors in computing the power ratio, all experiments, with only two exceptions (however characterized by values of Π very close to unity), are ebb dominated, thus, confirming previous observations (Aubrey & Speer, 1985; Friedrichs & Madsen, 1992). In fact, linear models predict that for values of the relative tidal amplitude ϵ greater than 0.3 flood dominance should be expected whereas the presence of tidal flats induces the flow to be ebb dominated (Friedrichs & Aubrey, 1988; Fortunato & Oliveira, 2005). Fortunato and Oliveira (2005) showed that tidal asymmetry and, thus, flood/ebb dominance, depends not only on the relative tidal amplitude, but also on the depth ratio (tidal flats to main channel water depth) and on the ratio between the main channel and tidal flats width. In general, results of Figure 5 suggest that ebb dominance increases as the friction parameter increases.

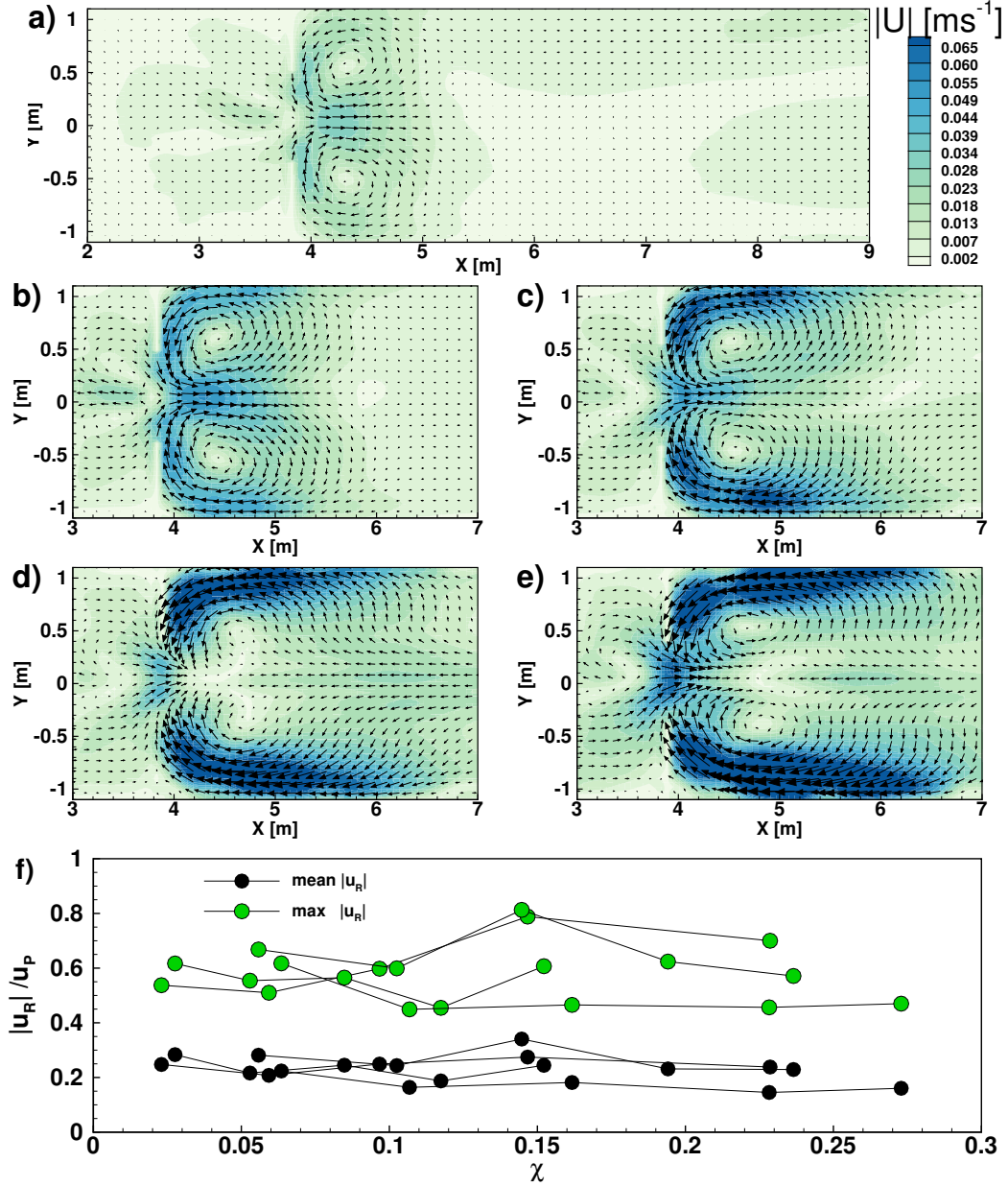


Figure 6. Panels from a) to e): examples of free surface residual current fields for the experiments from 13 to 17. Panel f): ratio of mean and max residual current velocity compared to the peak tidal velocity as a function of the parameter χ .

4.2 Shape and intensity of the residual current

In the previous section we have described the time dependent 2D velocity fields generated by the monochromatic tidal oscillation and the consequent generation of large scale vortical structures. We have also commented on the transient nature of the above macrostructure. Indeed the flood-vortices grow and disappear in a single tidal cycle. However, it is well known that the periodic oscillations due to tides not only generate a time dependent flow, but also a steady current known as residual current. As far as the any kind (sediment, nutrients and biogeochemicals) mass transport, it becomes relevant after sev-

eral tidal cycles and this is mainly due to the appearance of the residual currents, often referred to as “tidal pumping” that may lead to significant longitudinal dispersion (Zimmerman, 1986; Jay, 1991; Banas et al., 2004; Valle-Levinson, 2010).

The free surface residual current can be obtained averaging the time dependent free surface velocity fields over a tidal period, decomposing the velocity fields as: $\mathbf{u}(\mathbf{x}, t) = \mathbf{u}'(\mathbf{x}, t) + \mathbf{U}(\mathbf{x})$, where $\mathbf{U}(\mathbf{x})$ represents the Eulerian free surface residual current, no longer time dependent (Jay, 1991), and the $\mathbf{u}'(\mathbf{x}, t)$ is still a time dependent velocity field that could be, in principle, further averaged over a typical Eulerian integral scale to filter out the turbulent fluctuations (Valle-Levinson, 2010). In general, the net advection associated with tides may also vanish and the only net mass transport is then related to the residual current.

Figures 6a)- 6e) report the velocity vectors with superimposed contour plot for the magnitude ($|\mathbf{U}(\mathbf{x})|$) of the 2D free surface residual current for a sequence of experiments characterized by the same tidal period and different tidal amplitudes. Note that only a portion of the entire domain is represented in the aforementioned Figure. As a general comment, we observe that the resulting Eulerian residual current is perfectly symmetrical with respect to the main channel, as expected in a symmetrical domain. The flow pattern is quite regular away from the inlet mouth and mainly governed by the presence of two macro-vortices on the tidal flats and of smaller vortical structures on the basin side. The normalized tidal amplitude ϵ increases from panel a) to panel e) influencing both intensity and shape of the residual current. Indeed, intensity and dimension of the tidal flats macro-vortices increase as ϵ increases. Variations of the tidal period are less relevant in this case as the generation of the residual current is mainly due to the tidal amplitude (maps of the residual current at different periods are uploaded as additional material). Depending on the controlling parameters, the intensity of the residual current could reach values up to the 80% of the maximum velocity registered in the unsteady field. In Figure 6 panel f) we have reported the ratios of both the peak velocity of the residual current, defined as the mean of the 10% of the maximum measured values, and the mean residual current velocity with the peak tidal velocity measured at the inlet. The shape of the fields of $\mathbf{U}(\mathbf{x})$ is strongly related to the macro structures presented in the previous section. It seems that the transient flood-vortices averaged over a tidal cycle leave their signature in the generation of the residual current. The stream-wise extension of the vortical structures shown in Figures 6a)- 6e) is identical to the maximum size of the flood-vortices during the flood phase. It is worth noting that we are taking the measurements of the free surface velocities and this is somehow acceptable since the flow can be regarded as mainly 2D. However, by continuity, the time dependent flow and, thus, also the residual current is a 3D field. Regarding the residual current this implies that mass conservation is satisfied imagining that at both ends of the flume the flow is 3D and that, at the bottom, the flow is reversed compared to the free surface layer. Finally, we expect that the measured residual current strongly impacts on the Lagrangian mass transport and, ultimately, on the dispersion regimes. Zimmerman (1986) already noted the importance of the residual currents on the mass transport and that, in some cases, the complexity of the flow patterns may lead to chaotic mixing (Ridderinkhof & Zimmerman, 1992; Beerens et al., 1994) and the appearance of complex fluid deformation patterns that nowadays are recognized as Lagrangian coherent structures (Orre et al., 2006).

5 Lagrangian analysis and dispersion regimes

One of the main goals of the present study is to assess the dispersion processes occurring in weakly dissipative tide dominated estuaries characterized by the presence of an inlet mouth and a tidal channel with lateral flats. To this end, we started from the Eulerian velocity fields ($\mathbf{u}(\mathbf{x}, t)$), described in the previous sections, and computed numerical trajectories of material particles by integrating $\dot{\mathbf{x}}(t) = \mathbf{u}(\mathbf{x}, t)$ using a fourth-order Runge-Kutta algorithm with adaptive step size. About 2×10^4 trajectories have

been computed, from a regular grid seeding over a 10 m \times 2 m region of the total measuring domain. Computing numerical trajectories based on measured or computed Eulerian velocity fields is a practice commonly adopted in dispersion studies, see among others Lekien et al. (2005), Stocchino et al. (2011) and Enrile et al. (2020).

The numerical particle trajectories is then employed to estimate single particle statistics (LaCasce, 2008). In particular, we define the absolute dispersion $\mathbf{A}^2(t)$ and its trace, the total absolute dispersion $a^2(t)$, as:

$$A_{ij}^2(t) = \frac{1}{M} \sum_{m=1}^M \{ [x_i^m(t) - x_i^m(t_0)] [x_j^m(t) - x_j^m(t_0)] \} \quad a^2(t) = Tr(\mathbf{A}) \quad (2)$$

where M is the number of particles and $\mathbf{x}^m(t)$ is the position of the m -th particle at time t and $\mathbf{x}^m(t_0)$ its initial position. Note that the time derivative of $a^2(t)$ provides the estimate of the total absolute diffusivity coefficient $K^{(1)}(t)$ (Provenzale, 1999; LaCasce, 2008). Classical dispersion regimes are identified based on the time dependence of the total absolute dispersion following the theory of Taylor (1921), found to be valid in several geophysical context (LaCasce, 2008). The so-called Lagrangian integral scale T_{L_i} separates the quadratic and the linear time dependence of the absolute dispersion. It is defined as the time integral of the Lagrangian autocorrelation function of the i -th Lagrangian velocity component u_{L_i} as:

$$T_{L_i} = \int_0^{+\infty} \mathcal{R}_{ii} d\tau \quad \mathcal{R}_{ii}(\tau) = \frac{1}{M} \sum \frac{\rho_{L_{ii}}(\tau)}{\sqrt{\rho_{L_{ii}}(0)\rho_{L_{ii}}(0)}} \quad \rho_{L_{ii}}(\tau) = \langle u_{L_i}(t)u_{L_i}(t+\tau) \rangle. \quad (3)$$

where the brackets indicate an average over the entire duration of each trajectory and u_{L_i} is the i -th component of the Lagrangian velocity. In the rest of this section, we will present the main results obtained from the experimental measurements in terms of the above quantities discussing, in particular, the different dispersion regimes (Taylor, 1921).

5.1 Lagrangian Integral Scales

We start our analysis showing the computed autocorrelation functions and the corresponding Lagrangian integral time scales. The shape of the correlation function and their integral, namely the Lagrangian Integral Scale, are strongly related to the expected dispersion regimes (Taylor, 1921).

Figure 7 shows the autocorrelation functions \mathcal{R}_{uu} (panel a) and b)) and \mathcal{R}_{vv} (panel c)) as functions of the normalised time, along with the corresponding Lagrangian time scale T_L normalized with the tidal period T as a function of the relative tidal amplitude ϵ (panel d)) and of the parameter χ (panel e)), for all experiments. The flow is mainly unidirectional as shown by the rapidly decaying of the spanwise autocorrelation \mathcal{R}_{vv} ; thus, providing a small contribution to the overall value of T_L . The streamwise autocorrelation functions show a strong looping-like shape in all cases. The intensity of the negative and positive lobes is inversely dependent on the relative tidal amplitude ϵ (panel a)) for a fixed period. This is consistent with the fact that the periodic flow intensifies as the amplitude increases, leading to a decrease in the \mathcal{R}_{uu} . Tidal period variations for a fixed amplitude produce smaller difference in the streamwise autocorrelation structure, see panel b). The integral time scales show monotonic decrease as the relative amplitude increases, and hence the friction parameter increase, see panel d) and e). The values of T_L are found to be in a range between 0.03 and 0.38 T for values of ϵ between 0 and 0.2, and characterized by a rapid exponential decrease with the relative amplitude ϵ , for small values of the latter parameter. Interestingly, it seems that the Lagrangian integral scale attains an almost constant value for $\epsilon > 0.1$ (or $\chi > 0.15$). The fact that T_L is always smaller than the tidal period T implies that a diffusive regime, where the absolute dispersion depends linearly on time and a diffusivity coefficient can be defined, is likely to occur after a much shorter time compared to the external time scale (T). This also means

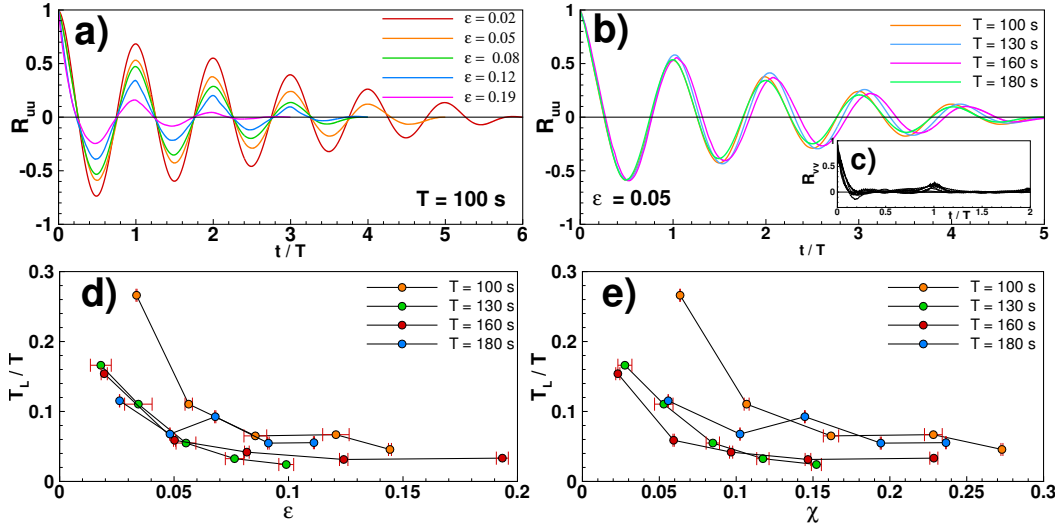


Figure 7. Lagrangian autocorrelation functions and integral time scales as a function of the tidal amplitude, period and the parameter χ . a) longitudinal autocorrelation function \mathcal{R}_{uu} for varying non dimensional tidal amplitude ϵ for a fixed value of the tidal period $T = 100$ s. b) longitudinal autocorrelation function \mathcal{R}_{uu} for varying tidal period for a fixed value of non dimensional tidal amplitude $\epsilon = 0.05$. c) spanwise autocorrelation function \mathcal{R}_{vv} for all experiments. d) Non dimensional Lagrangian integral time scale T_L/T as a function of the non dimensional tidal amplitude ϵ . e) Non dimensional Lagrangian integral time scale T_L/T as a function of the parameter χ .

that the tidal period is a good choice as a reference external scale for estuary classification (Toffolon et al., 2006) but less significant to discriminate among the different dispersion regimes. A decorrelation time smaller than the tidal period has also been found in dispersion analysis based on field data (Enrile et al., 2019). However, the periodicity imposed by the tidal forcing could be responsible for the looping-like behavior of \mathcal{R}_{uu} and, as we will see in the next section, it might also affect the long time behavior of the total absolute dispersion $a^2(t)$. Note that looping autocorrelation could be triggered also by the presence of large scale vortical structures as noted in Berloff et al. (2002) and Veneziani et al. (2004).

5.2 Single particle statistics and dispersion coefficients

This section represents the core of the present study. Indeed, our main interest was to understand the possible dispersion regimes that a monochromatic tide is able to sustain in a relatively complex geometry as the one used in the present physical model. Longitudinal dispersion is known to be produced or influenced by several mechanisms such as shear dispersion owing to periodical flows, macro-vortices and a steady residual current. We have seen how the interaction between a periodic tidal forcing, an inlet mouth and a compound channel triggers a fairly complex flow where all the latter mechanisms are active. The topological analysis of the flow based on the Okubo-Weiss criterion enlightened the presence of both elliptical (vortices at different scales) and hyperbolic regions (intense shear structures) in the domain with a markedly non-stationary character. It is worth mentioning that we have performed the single particle statistics analysis, see equations 2, starting from two different Eulerian velocity fields, namely the complete unsteady field $(\mathbf{u}(\mathbf{x}, t))$ and the associated residual current $(\mathbf{U}(\mathbf{x}))$. The reason will be clear when we will discuss the time behavior of $a^2(t)$. A second important prelimi-

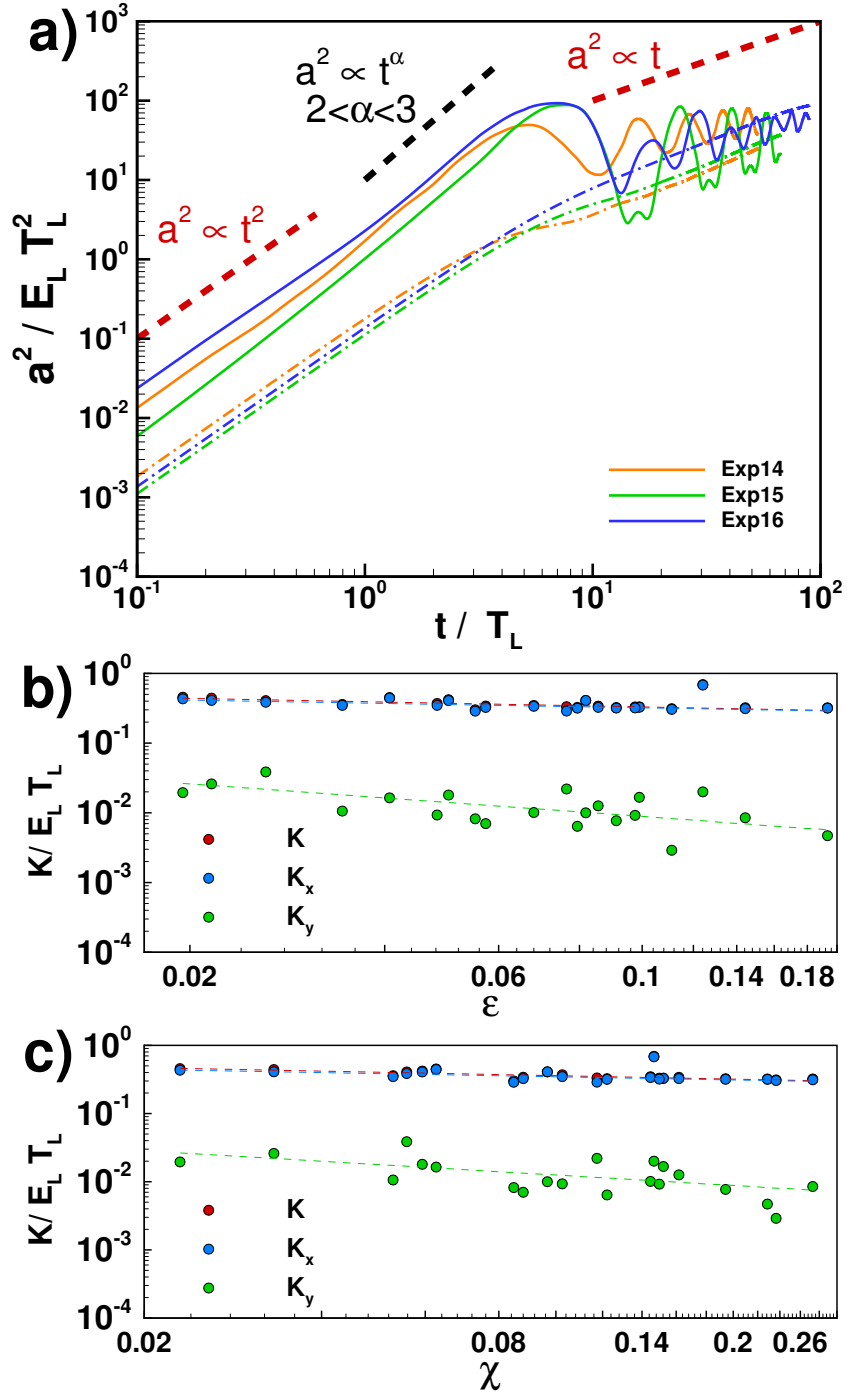


Figure 8. a) Examples of the non dimensional absolute dispersion $a^2(t)/(E_L T_L^2)$ as a function of non dimensional time t/T_L for experiments 14, 15 and 16, dotted lines indicates the found time laws for the dispersion regimes, dash-dotted lines the absolute dispersion derived from the residual current fields. b) Non dimensional horizontal dispersion coefficients $(K, K_x, K_y)/(E_k T_L)$ as a function of the non dimensional tidal amplitude ϵ . c) Non dimensional horizontal dispersion coefficients $(K, K_x, K_y)/(E_k T_L)$ as a function of the parameter χ . Dotted lines in panels b) and c) represent the fitting laws reported in 5.

nary comment refers to the kind of dispersion coefficients (K) we are going to estimate. As noted by Besio et al. (2012) the output of the single particle statistics analysis might produce coefficients that are related to several mixing processes and this depends on the starting Eulerian field assumed to compute the trajectories of numerical particles. In the present case, the only flow decomposition that we have performed is an average over the tidal period in order to generate the residual fields and no other averages have been performed (e.g. a moving average of the unsteady fields to isolate turbulent fluctuations). This means that our procedure yields to the estimate of a longitudinal coefficient (K_x), a transverse coefficient (K_y) and a total diffusive coefficient ($K = K_x + K_y$) that include also the turbulent diffusion contribution. All the dispersion properties will be presented in non dimensional form using as scaling quantity the ensemble averaged Lagrangian kinetic energy per unit mass $E_L = 1/2\langle(u_L(\mathbf{x}, t)^2 + v_L(\mathbf{x}, t)^2)\rangle$ and the Lagrangian integral scale T_L . Figure 8 summarizes results of the single particle statistics for the entire set of experiments. Panel a) displays the typical behavior of the time dependence of the non dimensional absolute dispersion $a^2(t)/(E_L T_L^2)$ for the unsteady velocity case (solid lines) and for the residual current case (dash-dotted lines) against the non dimensional time t/T_L in three experiments taken as an example (exp. 14, 15 and 16). Considering the results for the absolute dispersion computed with the time dependent Eulerian fields, different regimes are visible depending on the time. For time lower than T_L a ballistic regime is observed and, then, for $\mathcal{O}(t/T_L) \sim 1$ a super diffusive regime appears and lasts for few integral time scales. Super diffusive regimes are usually related to intense positive lobes in the auto-correlation functions (Berloff et al., 2002; Veneziani et al., 2004), as also observed in the present experiments. High anticorrelation is observed in all experiments, see Figure 7 panel a) and b), after the first zero of \mathcal{R}_{uu} regardless the controlling parameters and this yields to a regime where $a^2(t)/(E_L T_L^2) \propto (t/T_L)^\alpha$ with $\alpha \simeq 2-3$. For longer times, $t/T_L > 10$, the non dimensional absolute dispersion shows an oscillating behavior with a periodicity proportional to the tidal period. Interestingly, the oscillations hide a linear growth in time that is revealed by the absolute dispersion computed using the residual current alone (dash-dotted lines). Indeed, for each experiment, $a^2(t)/(E_L T_L^2)$ computed using the field $\mathbf{U}(\mathbf{x})$ seems to smooth out the super diffusive regime and the oscillations for longer times, displaying the standard picture of a ballistic regime for time lower than few T_L and a diffusive (linear regime) for longer times. The net advection associated with the periodical velocity components is negligible and particles are transported mainly by the residual currents that dominate, over long time, the dispersion process. The dispersion coefficients (K, K_x, K_y) have been calculated performing a linear regression of the non dimensional absolute dispersion for times $t/T_L > 10$. The obtained values, scaled by $E_L T_L$, are plotted in Figure 8 as a function of the relative tidal amplitude (ϵ), panel b), and as a function of the external parameter χ , panel c). Note that the data are reported in a log-log plane. Not surprisingly the greater contribution is given by the longitudinal coefficient K_x that turns out to be two order of magnitudes greater than the spanwise coefficient K_y . The dimensionless dispersion coefficients can be nicely grouped along a power law trend with both ϵ and χ . Using a least square fitting, we have obtained the following relations:

$$\begin{aligned} \frac{K}{E_L T_L} &= 0.2204\epsilon^{-0.1756}, & \frac{K_x}{E_L T_L} &= 0.2233\epsilon^{-0.1574}, & \frac{K_y}{E_L T_L} &= 0.0019\epsilon^{-0.6682}; & (4) \\ \frac{K}{E_L T_L} &= 0.2437\chi^{-0.1683}, & \frac{K_x}{E_L T_L} &= 0.2425\chi^{-0.1542}, & \frac{K_y}{E_L T_L} &= 0.0039\chi^{-0.5086} & (5) \end{aligned}$$

The goodness of fit R^2 ranges from 0.48, for the K_y , to about 0.7 for the coefficients K and K_x . The good fit obtained confirms that the choice of χ as a controlling external parameter is suitable not only for the hydrodynamic characterization of the estuaries (Toffolon et al., 2006) but also to globally describe the asymptotic dispersion regimes. Moreover, the results suggest that for increasing friction parameter the non dimensional coefficients tend to become almost constant and this is consistent also with results obtained in river dispersion, whereas for increasing friction the dispersion coefficients tend to be independent from the friction parameters itself (Webel & Schatzmann, 1984; Chau, 2000; Be-

sio et al., 2012). For increasing χ , $K/(E_L T_L)$ and its main contribution $K_x/(E_L T_L)$ tend to a value around 0.2-0.3 which is consistent with the measurements reported in the cited works. It is now important to understand how the present experimental estimates can be translated to realistic estuaries. Indeed, the observed values of K must be conveniently rescaled in the prototype (an equivalent system with real estuaries dimensions). To this end, let us denote by λ_V and λ_H the scaling factors for velocity and flow depth, respectively defined as the ratio between the typical scale of velocity and flow depth in the prototype and in the laboratory model. Hence, the scaling factor for the dispersive coefficients turn out to be $\lambda_K = \lambda_V^{\frac{1}{2}} \lambda_H$. Noting that the scaling factor for the velocity, can be defined as the ratio between the scaling factors of longitudinal length and time, and setting the time scaling factor in order to represent a semidiurnal or diurnal tide and using typical length scale of estuaries as reported in several works (Seminara et al., 2010; Toffolon et al., 2006; Zhang & Savenije, 2017), we are able to built λ_K and, therefore, to rescale the experimental estimates to reality. Depending on the controlling parameters, the present measurements suggest values of K in a range between 10^2 and $10^3 \text{ m}^2\text{s}^{-1}$. Large variability in the diffusion coefficient is commonly observed in field measurements in real estuaries with values comparable with our estimates (Fischer et al., 1979; Monismith et al., 2002; Lewis & Uncles, 2003; Banas et al., 2004). Several Authors also report a strong variability of the longitudinal coefficient K_x with the distance from the inlet, with larger values occurring near the ocean (Banas et al., 2004). In order to take into account for this variability, simple scaling has been proposed such as $K_x/(Ub) = c_k$ where U is a scale for the tidal induced velocity, b is the estuary width and c_k is a constant estimated by a regression over the measurements. Banas et al. (2004) suggested that the constant should assume values in a range between 0.05 and 0.1. This scaling is based on a conceptual model where the major agents of dispersion are thought to be the macrovortices generated by the residual current (MacCready, 1999) that, as in the present experiments, scale with the channel width. If we treat the present data using this simple model, we obtain for the constant c_k a median value equal to 0.023 and an estimate of the first (25th) percentile and third (75th) percentile equal to 0.020 and 0.035, respectively, which is fairly closed to the expected value. In real estuaries, this and other similar scaling were suggested in order to take into account for the spatial variability along the estuary. In fact, different mechanisms could modify the value of the longitudinal dispersion coefficient depending on the local hydrodynamics. The proposed relationship based on the external friction parameter should, instead, describe the global response of an estuary without considering a spatial dependency of the coefficient. Note that the absolute dispersion shown in Figure 8 is based on a uniform initial deployment of numerical particles and, thus, it describes the dispersion processes averaged over the entire domain, disregarding local non-homogeneities.

6 Conclusions

In this first part of the study, we have reported the results obtained using a single constituent tidal forcing on a large scale physical model of a basin (open ocean) connected to a compound tidal channel through the presence of a barrier island. Large scale PIV measurements of the 2D superficial time dependent velocity fields provided a huge data set upon which a thorough Eulerian and Lagrangian analysis has been performed. Flood-macrovortices are invariably observed for all experimental parameters. They are clearly generated by the presence of the inlet mouth and are able to occupy the entire tidal flats. An interesting process about the macro-vortices generation is the clear merging observed. This aspect, beyond the scope of the present study, would surely deserve a detailed analysis for its important consequence on the turbulent energy cascade and, thus, on the closure model of turbulent processes, especially momentum fluxes. Moreover, the compound geometry seems to sustain the generation of vorticity not only around the inlet, but also along the main channel transition zone (boundary with the tidal flats) forming transient vortical structures. In all cases, the flood-vortices are flushed out dur-

ing the ebb phase regardless the Strouhal number. This apparent discrepancy with previous studies (Wells & van Heijst, 2004; Nicolau del Roure et al., 2009) could be ascribed by the role of the compound geometry. Another striking Eulerian flow feature is the generation of an intense residual current, the shape of which is a reminiscence of the transient flood-vortices. Both the latter hydrodynamic features dominate the mixing process forced by a single harmonic tide. Two sources of periodicity seem to play an important role in defining the shapes of the Lagrangian autocorrelation functions and, ultimately, the dispersion regimes. Looping-like streamwise autocorrelations showed important negative lobes, soon after the first zero-crossing, forcing the system to respond with a super-diffusive regime, after a first short ballistic regime, that lasts for few Lagrangian integral time scales. For the range of external parameters investigated herein, a diffusive (Brownian) regime is always observed allowing for an estimate of horizontal dispersive coefficients. The present estimates confirm the order of magnitudes of dispersive coefficients observed in the field and also their great variability. Moreover, the results suggest that the *external* parameter χ may successfully represent most of the observed variability. This is further demonstrated by the reasonably good fitting laws here suggested. We leave to the companion Part 2, the investigation of the effects of multiple harmonics on the flow field and dispersion processes. This second part of the study will allow to extend our analysis to more realistic contexts where more likely tidal flow is generated by the contemporary coexistence of semi-diurnal and diurnal constituents.

Acknowledgments

This research has not been supported by external funding. The Authors declare no conflict of interests. All results are based on large scale PIV measurements, owing to the excessive dimensions of the data set no web repository has been prepared. Data Management Repository available at doi: <https://doi.org/10.5281/zenodo.5006375>.

References

- Aubrey, D., & Speer, P. (1985). A study of non-linear tidal propagation in shallow inlet/estuarine systems part i: Observations. *Estuarine, Coastal and Shelf Science*, *21*(2), 185–205.
- Banas, N., Hickey, B., MacCready, P., & Newton, J. (2004). Dynamics of willapa bay, washington: A highly unsteady, partially mixed estuary. *Journal of Physical Oceanography*, *34*(11), 2413–2427.
- Beerens, S., Ridderinkhof, H., & Zimmerman, J. (1994). An analytical study of chaotic stirring in tidal areas. *Chaos, Solitons & Fractals*, *4*(6), 1011–1029.
- Berloff, P. S., McWilliams, J. C., & Bracco, A. (2002). Material transport in oceanic gyres. part i: Phenomenology. *Journal of Physical Oceanography*, *32*(3), 764–796.
- Besio, G., Stocchino, A., Angiolani, S., & Brocchini, M. (2012). Transversal and longitudinal mixing in compound channels. *Water Resources Research*, *48*(12).
- Blondeaux, P., & Vittori, G. (2020). Modeling transverse coastal bedforms at anna maria island (florida). *Journal of Geophysical Research: Oceans*, *125*(7), e2019JC015837.
- Brocchini, M., & Colombini, M. (2004). A note on the decay of vorticity in shallow flow calculations. *Physics of Fluids*, *16*(7), 2469–2475.
- Cai, H., Savenije, H. H., & Toffolon, M. (2012). A new analytical framework for assessing the effect of sea-level rise and dredging on tidal damping in estuaries. *Journal of Geophysical Research: Oceans*, *117*(C9).
- Chau, K. W. (2000). Transverse mixing coefficient measurements in an open rectangular channel. *Advances in Environmental Research*, *4*(4), 287–294.
- Cucco, A., Umgiesser, G., Ferrarin, C., Perilli, A., Canu, D. M., & Solidoro, C. (2009). Eulerian and lagrangian transport time scales of a tidal active coastal

- basin. *Ecological Modelling*, 220(7), 913–922.
- Davies, P. A., Dakin, J. M., & Falconer, R. A. (1995). Eddy formation behind a coastal headland. *Journal of Coastal Research*, 154–167.
- Dronkers. (2019). *Estuarine dispersion: dye experiments in the eastern scheldt scale model*. [http://www.coastalwiki.org/wiki/Estuarine dispersion: dye experiments in the Eastern Scheldt scale mode](http://www.coastalwiki.org/wiki/Estuarine_dispersion:_dye_experiments_in_the_Eastern_Scheldt_scale_mode).
- Enrile, F., Besio, G., & Stocchino, A. (2020). Eulerian spectrum of finite-time lyapunov exponents in compound channels. *Meccanica*, 55(9), 1821–1828.
- Enrile, F., Besio, G., Stocchino, A., & Magaldi, M. G. (2019). Influence of initial conditions on absolute and relative dispersion in semi-enclosed basins. *Plos one*, 14(7), e0217073.
- Fischer, H. B., List, J. E., Koh, C. R., Imberger, J., & Brooks, N. H. (1979). *Mixing in inland and coastal waters*. Academic press.
- Fortunato, A. B., & Oliveira, A. (2005). Influence of intertidal flats on tidal asymmetry. *Journal of Coastal Research*, 21(5 (215)), 1062–1067.
- Friedrichs, C. T., & Aubrey, D. G. (1988). Non-linear tidal distortion in shallow well-mixed estuaries: a synthesis. *Estuarine, Coastal and Shelf Science*, 27(5), 521–545.
- Friedrichs, C. T., & Madsen, O. S. (1992). Nonlinear diffusion of the tidal signal in frictionally dominated embayments. *Journal of Geophysical Research: Oceans*, 97(C4), 5637–5650.
- Geyer, W. R., & MacCready, P. (2014). The estuarine circulation. *Annual review of fluid mechanics*, 46, 175–197.
- Gisen, J. I. A., & Savenije, H. H. (2015). Estimating bankfull discharge and depth in ungauged estuaries. *Water Resources Research*, 51(4), 2298–2316.
- Jay, D. A. (1991). Green’s law revisited: Tidal long-wave propagation in channels with strong topography. *Journal of Geophysical Research: Oceans*, 96(C11), 20585–20598.
- Jirka, G. (2001). Large scale flow structures and mixing processes in shallow flows. *J. Hydr. Res.*, 39, 567–573.
- Kang, J., & Jun, K. (2003). Flood and ebb dominance in estuaries in korea. *Estuarine, Coastal and Shelf Science*, 56(1), 187–196.
- Kusumoto. (2008). *Laboratory experiments of tidal dispersion around irregular boundaries*. Phd Thesis.
- LaCasce, J. (2008). Statistics from lagrangian observations. *Progress in Oceanography*, 77, 1-29.
- Lanzoni, S., & Seminara, G. (1998). On tide propagation in convergent estuaries. *Journal of Geophysical Research: Oceans*, 103(C13), 30793–30812.
- Lekien, F., Coulliette, C., Mariano, A., Ryan, E., Shay, L., Haller, G., & Marsden, J. (2005). Pollution release tied to invariant manifolds: A case study for the coast of florida. *Phys. D*, 210, 1–20.
- Lewis, R. E., & Uncles, R. J. (2003). Factors affecting longitudinal dispersion in estuaries of different scale. *Ocean Dynamics*, 53(3), 197–207.
- MacCready, P. (1999). Estuarine adjustment to changes in river flow and tidal mixing. *Journal of Physical Oceanography*, 29(4), 708–726.
- MacCready, P., & Geyer, W. R. (2009). Advances in estuarine physics.
- Monismith, S. G., Kimmerer, W., Burau, J. R., & Stacey, M. T. (2002). Structure and flow-induced variability of the subtidal salinity field in northern san francisco bay. *Journal of physical Oceanography*, 32(11), 3003–3019.
- Nicolau del Roure, F., Socolofsky, S. A., & Chang, K.-A. (2009). Structure and evolution of tidal starting jet vortices at idealized barotropic inlets. *Journal of Geophysical Research: Oceans*, 114(C5).
- Okubo, A. (1970). Horizontal dispersion of floatable particles in the vicinity of velocity singularities such as convergences. In *Deep sea research and oceanographic abstracts* (Vol. 17, pp. 445–454).

- Orre, S., Gjevik, B., & LaCasce, J. H. (2006). Characterizing chaotic dispersion in a coastal tidal model. *Continental Shelf Research*, *26*(12-13), 1360–1374.
- Pritchard, D. W. (1956). The dynamic structure of a coastal plain estuary. *J. Mar. Res.*, *15*(1), 33–42.
- Provenzale, A. (1999). Transport by coherent barotropic vortices. *Ann. Rev. Fluid Mech.*, *31*, 55–93.
- Ridderinkhof, H., & Zimmerman, J. (1992). Chaotic stirring in a tidal system. *Science*, *258*(5085), 1107–1111.
- Savenije, H. H. (1993). Determination of estuary parameters on basis of lagrangian analysis. *Journal of Hydraulic Engineering*, *119*(5), 628–642.
- Seminara, G., Lanzoni, S., Tambroni, N., & Toffolon, M. (2010). How long are tidal channels? *Journal of Fluid Mechanics*, *643*, 479.
- Signell, R. P., & Geyer, W. R. (1991). Transient eddy formation around headlands. *Journal of Geophysical Research: Oceans*, *96*(C2), 2561–2575.
- Stocchino, A., Besio, G., Angiolani, S., & Brocchini, M. (2011). Lagrangian mixing in straight compound channels. *Journal of Fluid Mechanics*, *675*, 168.
- Stocchino, A., & Brocchini, M. (2010). Horizontal mixing of quasi-uniform, straight, compound channel flows. *J. Fluid Mech.*, *643*, 425–435.
- Taylor, G. (1921). Diffusion by continuous movement. *Proc. Lond. Math. Soc.*, *20*, 196–212.
- Toffolon, M., Vignoli, G., & Tubino, M. (2006). Relevant parameters and finite amplitude effects in estuarine hydrodynamics. *Journal of Geophysical Research: Oceans*, *111*(C10).
- Umgiesser, G., Ferrarin, C., Cucco, A., De Pascalis, F., Bellafiore, D., Ghezzi, M., & Bajo, M. (2014). Comparative hydrodynamics of 10 mediterranean lagoons by means of numerical modeling. *Journal of Geophysical Research: Oceans*, *119*(4), 2212–2226.
- Valle-Levinson, A. (2010). *Contemporary issues in estuarine physics*. Cambridge University Press.
- Veneziani, M., Griffa, A., Reynolds, A. M., & Mariano, A. J. (2004). Oceanic turbulence and stochastic models from subsurface lagrangian data for the northwest atlantic ocean. *Journal of physical oceanography*, *34*(8), 1884–1906.
- Viero, D. P., & Defina, A. (2016). Water age, exposure time, and local flushing time in semi-enclosed, tidal basins with negligible freshwater inflow. *Journal of Marine Systems*, *156*, 16–29.
- Vouriot, C. V., Angeloudis, A., Kramer, S. C., & Piggott, M. D. (2019). Fate of large-scale vortices in idealized tidal lagoons. *Environmental Fluid Mechanics*, *19*(2), 329–348.
- Webel, G., & Schatzmann, M. (1984). Transverse mixing in open channel flow. *Journal of Hydraulic Engineering*, *110*(4), 423–435.
- Weiss, J. (1991). The dynamics of enstrophy transfer in two-dimensional hydrodynamics. *Physica D*, *48*, 272–294.
- Wells, M., & van Heijst, G. (2004). Dipole formation by tidal flow in a channel. In *International symposium on shallow flows*. balkema publishers, delft (pp. 63–70).
- Yang, Y., Chui, T. F. M., Shen, P. P., Yang, Y., & Gu, J. D. (2018). Modeling the temporal dynamics of intertidal benthic infauna biomass with environmental factors: Impact assessment of land reclamation. *Science of The Total Environment*, *618*, 439–450.
- Zhang, Z., & Savenije, H. H. (2017). The physics behind van der burgh’s empirical equation, providing a new predictive equation for salinity intrusion in estuaries. *Hydrology and Earth System Sciences*, *21*(7), 3287–3305.
- Zimmerman, J. (1986). The tidal whirlpool: a review of horizontal dispersion by tidal and residual currents. *Netherlands Journal of Sea Research*, *20*(2-3), 133–154.